BIOCHEMISTRY
including biophysical chemistry & molecular biology

Article

pubs.acs.org/biochemistry

$\alpha_V\beta_3$ Integrin Crystal Structures and Their Functional Implications

Xianchi Dong,[†] Li-Zhi Mi,[†] Jianghai Zhu,[†] Wei Wang,[‡] Ping Hu,[‡] Bing-Hao Luo,[†,‡] and Timothy A. Springer*[,†]

[†]Immune Disease Institute, Children's Hospital Boston, and Department of Biological Chemistry and Molecular Pharmacology, Harvard Medical School, 3 Blackfan Circle, Boston, Massachusetts 02115, United States

[‡]Department of Biological Sciences, 202 Life Sciences Building, Louisiana State University, Baton Rouge, Louisiana 70803, United States

Supporting Information

ABSTRACT: Many questions about the significance of structural features of integrin $\alpha_V\beta_3$ with respect to its mechanism of activation remain. We have determined and re-refined crystal structures of the $\alpha_V\beta_3$ ectodomain linked to C-terminal coiled coils ($\alpha_V\beta_3$-AB) and four transmembrane (TM) residues in each subunit ($\alpha_V\beta_3$-1TM), respectively. The α_V and β_3 subunits with four and eight extracellular domains, respectively, are bent at knees between the integrin headpiece and lower legs, and the headpiece has the closed, low-affinity conformation. The structures differ in the occupancy of three metal-binding sites in the βI domain. Occupancy appears to be related to the pH of crystallization, rather than to the physiologic regulation of ligand binding at the central, metal ion-dependent adhesion site. No electron density was observed for TM residues and much of the α_V linker. $\alpha_V\beta_3$-AB and $\alpha_V\beta_3$-1TM demonstrate flexibility in the linker between their extracellular and TM domains, rather than the previously proposed rigid linkage. A previously postulated interface between the α_V and β_3 subunits at their knees was also not supported, because it lacks high-quality density, required rebuilding in $\alpha_V\beta_3$-1TM, and differed markedly between $\alpha_V\beta_3$-1TM and $\alpha_V\beta_3$-AB. Together with the variation in domain−domain orientation within their bent ectodomains between $\alpha_V\beta_3$-AB and $\alpha_V\beta_3$-1TM, these findings are compatible with the requirement for large structural changes, such as extension at the knees and headpiece opening, in conveying activation signals between the extracellular ligand-binding site and the cytoplasm.

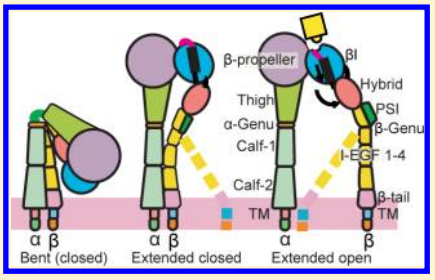

Integrins have noncovalently associated α- and β-subunits, each with an ectodomain (~1000 residues in α and ~700 in β), a single transmembrane domain, and a typically short cytoplasmic domain. Integrin ectodomains have four domains in α and eight in β, of which one in each associates tightly to form a ligand-binding head (Figure 1). The remaining domains connect the heads through upper legs, knees, and lower legs to the plasma membrane. In the bent conformation, the knees are bent and the headpiece (head and upper legs) folds over the lower legs to form a 2000 Å^2 interface (Figure 1A). In two extended conformations, the legs are extended at the knees and the headpiece may be either closed, as in the bent conformation, or open (Figure 1B,C). Headpiece opening involves a large conformational change at the hybrid domain interface where the βI domain is inserted, i.e., attached at both its N- and C-termini. Headpiece opening is conveyed by α-helix-connecting rodlike movements across the βI domain to its interface with the α-subunit where the ligand is bound and increases the affinity for the ligand by many orders of magnitude (Figure 1C). Most integrins interact with the actin cytoskeleton and transmit signals in both directions across the membrane to regulate binding to extracellular ligands and traction through the cytoskeleton for cell migration and signaling.[1]

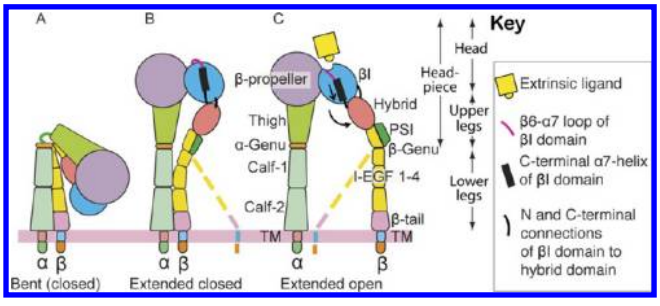

Figure 1. Three major integrin conformational states: (A) bent (with a closed headpiece), (B) extended with a closed headpiece, and (C) extended with an open headpiece. The dashed lower β-legs show that because of β-leg flexibility in the extended conformation, the closed and open headpieces are each compatible with TM domain close association and separation. However, a lateral force exerted by the cytoskeleton on the β-subunit can enforce TM domain separation and the open headpiece conformation.[1]

The key question in the integrin field is how signals are transmitted from integrin cytoplasmic and transmembrane domains to the ligand-binding site in the ectodomain to regulate affinity for the ligand. We and others have presented

Received: June 4, 2012
Revised: October 1, 2012
Published: October 29, 2012

   dx.doi.org/10.1021/bi300734n | *Biochemistry* 2012, 51, 8814−8828

extensive evidence of two key types of conformational changes: (1) integrin extension to give the extended−closed state (Figure 1B) and (2) integrin headpiece opening to give the extended−open state (Figure 1C).[1] The extended closed conformation has a low affinity for the ligand, and only the extended−open conformation has a high affinity.[2−9] Thus, integrin activation by inside-out signals increases the proportion of integrins with the extended−open conformation. These conclusions are supported by a large number of electron microscopy (EM), small-angle X-ray scattering (SAXS), and crystallographic studies as well as affinity measurements on cell surfaces. The studies include work on diverse integrins, including $\alpha_V\beta_3$, $\alpha_{IIb}\beta_3$, $\alpha_5\beta_1$, $\alpha_V\beta_6$, $\alpha_L\beta_2$, and $\alpha_X\beta_2$.[1] To communicate allostery over unusually large distances through the flexible lower leg of the β-subunit in the extended conformation, it has been emphasized that large separations between the integrin transmembrane and cytoplasmic domains would be required, and evidence of such separation has been obtained by transmembrane domain cross-linking and fluorescence resonance energy transfer (FRET) experiments.[10−12]

On the other hand, another model proposes that integrin activation requires neither extension nor headpiece opening.[13,14] The body of evidence supporting this alternative model is smaller and is based on studies of integrin $\alpha_V\beta_3$.[13,14] Crucial in the latest support for this hypothesis was a crystal structure of integrin $\alpha_V\beta_3$.[14] Excellent density was reported for the ectodomain, as well as the first three residues of both the α_V and β_3 TM residues. It was unexpected that the α_V and β_3 TM residues were far from one another in the crystal structure (25 Å), because structures for the closely related α_{IIb} and β_3 TM domains show the same residues in close contact.[15−17] Nonetheless, a model was made by bending the ectodomain−TM linkers in both α_V and β_3 to bring the TM domains close, and it was suggested that some rigidity in the linker region is essential to maintain the integrin in its inactive conformation.[14] Linker rigidity sets $\alpha_V\beta_3$ apart from integrins $\alpha_{IIb}\beta_3$ and $\alpha_X\beta_2$. Ectodomain−TM domain linkers were disordered in $\alpha_{IIb}\beta_3$ and $\alpha_X\beta_2$ crystal structures, suggesting flexibility.[18,19] Furthermore, disulfide cross-linking of the α_{IIb} and β_3 linkers on intact $\alpha_{IIb}\beta_3$ on cell surfaces demonstrated a lack of a specific interface.[15]

Several other features of $\alpha_V\beta_3$ crystal structures appear to be unusual. The βI metal ion-dependent adhesion site (MIDAS) is located between two other divalent metal-binding sites, the adjacent to MIDAS (ADMIDAS) and synergistic metal-binding site (SyMBS). $\alpha_V\beta_3$ was found to lack metal ions at the MIDAS and SyMBS but to contain them when a ligand was soaked in, and metal ions were thought to regulate ligand binding.[14,20] In contrast, $\alpha_{IIb}\beta_3$, with an identical β-subunit, binds metal ions at all three sites in the absence of a ligand.[18,21] $\alpha_V\beta_3$ has been reported to have clear density at its β-knee,[14] in contrast to $\alpha_{IIb}\beta_3$.[18] A specific, stabilizing interface between the α_V and β_3 knees was reported that is unusual for one containing many hydrogen bonds between highly solvent accessible carbonyl and carboxyl groups.[14] Such carboxyls are considered to be deprotonated at physiologic pH, and interactions between oxygen lone pair electrons are highly unfavorable. A specificity-determining loop (SDL) in the βI domain of the β_3 subunit near the ligand-binding interface with the α-subunit was built markedly differently in a 2004 $\alpha_{IIb}\beta_3$ crystal structure[4] than in the 2001 $\alpha_V\beta_3$ crystal structure.[22] The conformation in $\alpha_V\beta_3$ was retained in the 2009 crystal structure,[14] perhaps implying an influence of the α-subunit on the conformation of the nearby SDL in β_3.

To obtain an independent view of integrin $\alpha_V\beta_3$, we have determined a structure of its ectodomain fused to coiled-coil peptides to mimic associating TM α-helices ($\alpha_V\beta_3$-AB). Furthermore, to better address special issues raised by the $\alpha_V\beta_3$-1TM structure, we carefully examined this structure and its underlying electron density. After doing so, we decided that it would benefit from re-refinement. Therefore, we report here two different $\alpha_V\beta_3$ crystal structures. Using these structures and their objective electron density, we report several novel structural features and come to novel conclusions about the bent−closed structure of $\alpha_V\beta_3$ and its implications for activation.

MATERIALS AND METHODS

Clasped $\alpha_V\beta_3$-AB Ectodomain Structure. The α_V ectodomain sequence ending at M960 was fused to sequences in the order GSGGEN and AQCEKELQALEKENAQLEWELQALEKELAQ, corresponding to a six-residue vector-derived sequence and the ACID-p1 sequence of peptide Velcro[23] containing a Cys at the "d" position of the heptad repeat,[24] respectively. The β_3 ectodomain sequence ending at P691 was fused to sequences in the order ESM, LENLYFQ, GGKN, AQCKKKLQALKKKNAQLKWKLQALKKKLAQ, TG, and HHHHHH, corresponding to a three-residue linker, a tobacco etch virus (TEV) protease site, a four-residue linker, the BASE-p1 sequence of peptide Velcro[23] containing a Cys at the "d" position of the heptad repeat,[24] a two-residue linker, and a His_6 tag, respectively.[2] Protein was expressed in CHO Lec 3.2.8.1 cells,[2] purified from the culture supernatant using Ni-NTA agarose (QIAGEN) followed by gel filtration (Superdex 200 HR) chromatography in 0.01 M Tris-HCl (pH 7.5), 0.14 M NaCl (TBS), and 1 mM Ca^{2+}, and concentrated to ~5.5 mg/mL.

Crystals from hanging-drop vapor diffusion at room temperature were in 2 M ammonium sulfate, 80 mM sodium cacodylate (pH 5.8), 2 mM $CaCl_2$, and 6 mM $MgCl_2$. Coverslips with their hanging drops were transferred to wells containing saturated ammonium sulfate for dehydration over 16 h. Crystals were cryoprotected in 95% saturated ammonium sulfate and 5% glycerol before being plunge-frozen in liquid nitrogen.

Diffraction data from GM/CA-CAT beamline 23-ID of Advanced Photon Source (APS) at Argonne National Laboratory were processed using XDS.[25] The structure was determined using molecular replacement with PHASER with both 3IJE and 4G1M $\alpha_V\beta_3$-1TM structures (described below). The rotation function and translation function Z scores were 15.0 and 26.5, respectively, for the 3IJE model and 16.2 and 38.1, respectively, for the 4G1M model. Initial structure refinement with PHENIX[26] used rigid bodies for individual domains, individual sites, TLS, and individual B factor refinement. Using the same parameters, we obtained R_{work} and R_{free} values of 27.4 and 33.7% with 3IJE and 24.4 and 31.4% with 4G1M, respectively. Like the better molecular replacement scores with the 4G1M model, these refinement results showed that the 4G1M $\alpha_V\beta_3$-1TM model fit better the $\alpha_V\beta_3$-AB data set than the 3IJE $\alpha_V\beta_3$-1TM model. The initial $\alpha_V\beta_3$-AB model obtained using replacement with the 4G1M $\alpha_V\beta_3$-1TM model was therefore used as the starting model for subsequent refinement.

After several rounds of manual model rebuilding with Coot[27] and refinement with PHENIX, simulated annealing was used in refinement instead of rigid body refinement. Simulated annealing composite omit maps were also calculated and used to guide manual rebuilding to decrease model bias. During

dx.doi.org/10.1021/bi300734n | Biochemistry 2012, 51, 8814−8828

Table 1. Statistics of X-ray Diffraction and Structure Refinement

	Data Collection[a]		
	$\alpha_V\beta_3$-AB		$\alpha_V\beta_3$-1TM
space group	$P3_221$		$P3_221$
α, β, γ (deg)	90, 90, 120		90, 90, 120
unit cell ($a = b, c$) (Å)	128.46, 352.49		130.26, 305.98
resolution range (Å)	50.0−2.85 (2.92−2.85)		65−2.9
completeness (%)	99.9 (100.0)		99.2 (98.5)
no. of unique reflections	79656 (5806)		66702 (6515)
redundancy	7.4 (6.6)		2.9 (2.2)
R_{sym} (%)	17.5 (457.6)		8.8 (100)
I/σ	10.2 (0.6)		10.5 (100)[b]
$CC_{1/2}$ (%)[c]	99.7 (13.6)		NA
wavelength (Å)	1.034		1.0332
	4G1E	3IJE	4G1M
Refinement			
resolution range (Å)	50.0−2.85	20−2.9	65−2.9
R_{work} (%)	24.1	24.4	18.0
R_{free} (%)	26.1	28.7	23.4
Model			
bond rmsd (Å)	0.005	0.006	0.005
angle rmsd (deg)	0.6	1.086	0.735
Ramachandran plot[d] (favored/allowed/outlier)	95.8/4.0/0.2	88.4/8.5/3.1	93.2/6.7/0.1
MolProbity percentile[d] (clashscore/geometry)	97/100	91/66	97/99
residue range			
α_V	1−619, 621−838, 841−848, 867−959	1−838, 868−967	1−837, 868−959
β_3	1−33, 35−478, 483−691	1−695	1−692
no. of metals	6	6	7
no. of carbohydrates	48	34	37
no. of *cis*-prolines	7	0	7
no. of waters	104	0	108

[a]The numbers in parentheses refer to data for the highest-resolution shell. [b]The number in parentheses cannot be correct but cannot be recalculated by us and is shown as originally reported. [c]Pearson's correlation coefficient between average intensities of random half-data sets of the measurements for each unique reflection.[28] [d]Calculated with the described server.[30]

iterative rebuilding and refinement, an 8% twin fraction was observed in the data set with the twin law $H, K, -L$. After the twin law had been applied, both R_{work} and R_{free} decreased ~1.5%. The ACID and BASE α-helical coiled-coil (leucine zipper) peptides, but not the linkers to the C-termini of the α_V and β_3 subunits, were present in electron density and were added to the model.

Refinement was first completed at 3.0 Å resolution. Using a recent cross-correlation method,[28] we found that useful data extended to 2.85 Å. Density improved, and refinement was extended to this resolution.

Refinement of 3IJE. We calculated simulated annealing (SA) composite omit maps using the $\alpha_V\beta_3$-1TM [Protein Data Bank (PDB) entry 3IJE] coordinates and structure factor amplitudes with both CNS[29] and PHENIX.[26] Neither program's SA omit maps showed 1σ electron density for a substantial portion of the β_3 I-EGF1 domain, portions of the I-EGF2 and PSI domains, much of the α-subunit linker, or the TM segments of the α- and β-subunits.

On the basis of these results, we started with a model lacking the PSI, I-EGF1, and I-EGF2 domains and systematically rebuilt the $\alpha_V\beta_3$ structure in 16 iterative steps of manual rebuilding with Coot,[27] attention to outliers and clashes identified with MolProbity,[30] and TLS and maximum-likelihood refinement with REFMAC.[31] PyMol scripts were used to superimpose individual domains from high-resolution $\alpha_{IIb}\beta_3$ structures to provide hints for rebuilding. At each step, we computed PHENIX simulated annealing composite omit maps.[26] The PSI and most of the I-EGF1 and I-EGF2 domains appeared in the $2F_o-F_c$ map during refinement and were added back. R_{free} decreased from 28.5% in 3IJE to 26.9%. Another SA omit map calculated with CNS showed most of the I-EGF1 domain.

Many further cycles of rebuilding in Coot utilized PHENIX refinement with TLS, maximum likelihood, and simulated annealing.[26] R_{free} decreased to 24.2%. Subsequent refinement cycles without simulated annealing resulted in a final R_{free} of 23.4%. In the last cycle, EGF-1 was carefully examined. Only short segments were missing in the 1σ $2F_o-F_c$ map; however, the overall quality of the map remained lower than for other domains, suggesting flexibility. A low-resolution map computed from data between ~65 and 3.7 Å was used to check this less ordered domain. This map clearly showed the *N*-acetylglucosamine residue attached to β_3 Asn-452, which was added back. The C-termini of α_V and β_3 were each extended approximately two residues past the last residue in the 1σ map, to the last peptide moiety in ~0.5σ density, beyond which there could be no confidence in the path of the polypeptide chain.

$\alpha_V\beta_3$ Furin Site Mutation and Function. Full-length human α_V and β_3 plasmids were subjected to site-directed mutagenesis and cotransfected into HEK293T cells as previously described.[2] Cell surface expression measured with nonfunctional Cy3-conjugated β_3 mAb AP3 and binding of Alexa-488-conjugated fibrinogen and fibronectin were assessed by fluorescence flow cytometry.[8] Briefly, transfected cells were

dx.doi.org/10.1021/bi300734n | *Biochemistry* 2012, 51, 8814−8828

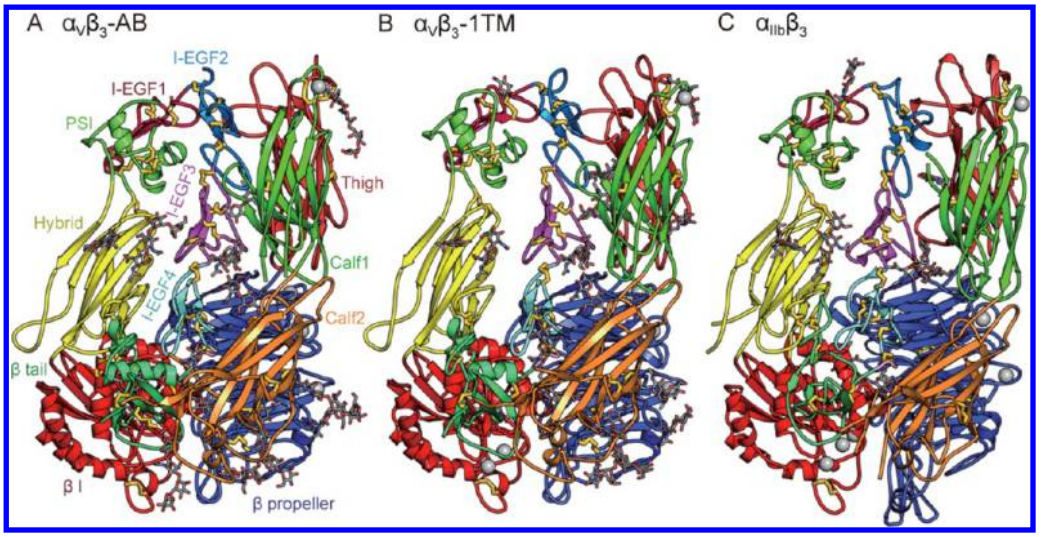

Figure 2. Overall structures of two $\alpha_V\beta_3$ crystal forms and comparison to $\alpha_{IIb}\beta_3$. (A–C) Cartoons of $\alpha_V\beta_3$-AB (A), $\alpha_V\beta_3$-1TM (4G1M structure, B), and $\alpha_{IIb}\beta_3$ (C). Ca^{2+} and Mg^{2+} ions are shown as silver spheres. Disulfides are shown as gold sticks, and glycans are displayed with gray carbons.

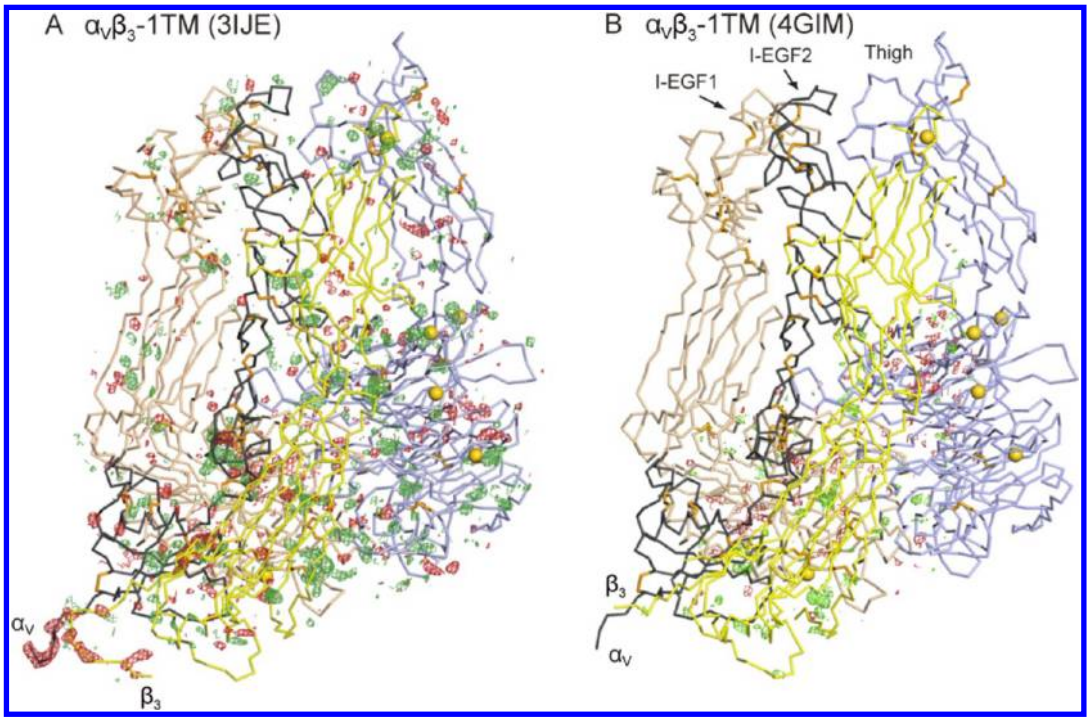

Figure 3. Difference maps of 3IJE (A) and 4G1M (B) $\alpha_V\beta_3$-1TM structures. F_o-F_c difference density is colored green ($+3\sigma$) and red (-3σ). The head and upper legs of α_V and β_3 are colored light blue and wheat, respectively, and the lower α_V and β_3 legs are colored yellow and black, respectively. The C-termini are labeled for α_V and β_3.

detached, resuspended in 20 mM HEPES-buffered saline (pH 7.4) (HBS), supplemented with 5.5 mM glucose and 1% bovine serum albumin, and incubated at room temperature for 30 min with human fibrinogen or fibronectin in the presence of either 5 mM EDTA, 5 mM Ca^{2+}, or 1 mM Mn^{2+}. Cells were then stained with Cy3-conjugated AP3 on ice for 30 min.

Transiently transfected cells were metabolically labeled with [^{35}S]cysteine/methionine and subjected to immunoprecipitation as described previously.[11] Lysates in 20 mM Tris-buffered saline (pH 7.4) (TBS), supplemented with 1 mM Ca^{2+}, 1% Triton X-100, 0.1% Nonidet P-40, and 1:100 (v/v) protease inhibitor cocktail (Sigma-Aldrich, St. Louis, MO), were immunoprecipitated with 1 μg of $\alpha_V\beta_3$ mAb LM609 (EMD Millipore Corp., Billerica, MA) and protein G-Sepharose at 4 °C for 1 h.

RESULTS

***$\alpha_V\beta_3$*-AB Ectodomain Structure.** Previously described $\alpha_V\beta_3$-ΔTM[22] and $\alpha_V\beta_3$-1TM proteins[14] were each expressed in insect cells, differ in length from one another by only four TM residues in each subunit, and crystallize with 10–12% PEG as the precipitant in nearly identical lattices. The space group is $P3_221$, and the unit cell dimensions are as follows: $a = b = 130.0$ Å ($\alpha_V\beta_3$-ΔTM) or 130.26 Å ($\alpha_V\beta_3$-1TM), and $c = 307.3$ Å ($\alpha_V\beta_3$-ΔTM) or 305.98 Å ($\alpha_V\beta_3$-1TM). Such small differences

dx.doi.org/10.1021/bi300734n | *Biochemistry* 2012, 51, 8814–8828

in lattice dimensions are typical for different crystals of the same protein.

To obtain an independent view of $\alpha_V\beta_3$ structure, we expressed in mammalian CHO-Lec cells the complete $\alpha_V\beta_3$ ectodomain, connected through 6-residue (α_V) and 14-residue (β_3) linkers to the ACID and BASE leucine zipper Velcro peptides[2,23] ($\alpha_V\beta_3$-AB). Crystals formed with a different class of precipitant, 2 M ammonium sulfate. The space group was still $P3_221$, and the a and b dimensions of 128.46 Å were similar to those of 130.26 Å for $\alpha_V\beta_3$-1TM; however, at 352.49 Å, the c dimension was markedly larger than the dimension of 305.98 Å for the previous crystals (Table 1). The structure includes the ACID−BASE leucine zipper; however, it has little if any effect on $\alpha_V\beta_3$ because the long linkers between the α_V and β_3 subunits and the ACID and BASE peptides are disordered. The 2.85 Å $\alpha_V\beta_3$-AB structure (Figure 2A) is well-refined, with an R_{free} of 26.2%, excellent Ramachandran and geometry statistics, and high MolProbity[30] percentiles (Table 1).

$\alpha_V\beta_3$-1TM Ectodomain Structure. The 2.9 Å $\alpha_V\beta_3$-1TM structure was determined by molecular replacement[14] and is therefore subject to model bias. The standard method for obtaining a less model-biased map is to compute an SA composite omit map.[32] Independent SA composite omit maps were calculated with CNS and PHENIX using the deposited $\alpha_V\beta_3$-1TM (PDB entry 3IJE) data. The maps showed absent or poor electron density for much of the PSI, I-EGF1, and I-EGF2 domains, the linker between the ectodomain and TM domains, and TM domain residues. Furthermore, difference map peaks showed a substantial number of places where the 3IJE model and the electron density did not correlate (Figure 3A, red and green mesh).

Therefore, we rebuilt the $\alpha_V\beta_3$-1TM molecular model using many iterative steps of rebuilding with Coot and refinement that included use of REFMAC, PHENIX, and SA. We initially omitted regions with poor density. As other domains improved, 1σ density for the PSI, I-EGF1, and I-EGF2 domains reappeared, and these domains were added back. We recalculated SA composite omit maps after each refinement step and used MolProbity to find clashes, bad rotamers, and Ramachandran outliers after each refinement. Density for C-terminal portions of α_V and β_3 did not reappear, and they are thus absent from the final model.

The new and previous $\alpha_V\beta_3$-1TM molecular models are cited here by their PDB entries, 4G1M and 3IJE, respectively. If the PDB entry is not specified, $\alpha_V\beta_3$-1TM refers to the 4G1M structure. The 4G1M structure has many fewer regions of disagreement with electron density (Figure 3B) than 3IJE (Figure 3A). Furthermore, 4G1M is refined against data from 2.9 to 65 Å, as opposed to 2.9 to 20 Å for 3IJE (Table 1). The greater amount of low-resolution data used in 4G1M allows better definition of less ordered regions, i.e., the PSI, I-EGF1, and I-EGF2 domains (Figure 2B). Differences in the β_3 PSI, I-EGF1, and I-EGF2 domains [Cα rmsd of 1.2−1.4 Å (Table 2)] occur throughout their length, whereas differences in the larger integrin domains result primarily from rebuilding of loops. The rebuilding process resulted in a decrease in R_{free} from 28.5 to 23.4%, a decrease in the level of Ramachandran outliers from 3.1 to 0.1%, and a decrease in the level of poor rotamers from 7.9 to 0.6%, as reported by MolProbity[30] (Table 1).

Overall Structures. Both $\alpha_V\beta_3$ structures reveal an overall bent conformation (Figure 2A,B). The α_V β-propeller and β_3 βI domains interact over a large interface to form the integrin head and its ligand-binding site. Acute bends define the knees, at the junction between the upper and lower legs. The α_V leg is bent between the thigh and calf-1 domains, at the disulfide-bonded, Ca^{2+}-binding genu loop, or α-knee. The bend in β occurs at the β-genu between I-EGF domains 1 and 2. Thus, the thigh domain in α_V and the PSI, hybrid, and I-EGF1 domains in β_3 form the upper legs. The calf-1 and calf-2 domains in α_V and the I-EGF2, I-EGF3, and I-EGF4 domains, β-ankle loop, and β-tail domains in β_3 form the lower legs (Figure 1). Large interfaces are buried between the head and the lower legs, and between the α_V and β_3 legs, that stabilize the bent conformation.[2] Because structures of $\alpha_V\beta_3$[14,20,22,33] and $\alpha_{IIb}\beta_3$[4,18,21,34,35] have previously been described, we focus our attention on the most notable differences and the structural features that are relevant for models of integrin ligand binding and activation.

Table 2. Root-Mean-Square Deviations between 3IJE and 4G1M $\alpha_V\beta_3$-1TM Structures[a]

domain	residues	3IJE/4G1M for non-H atoms (Å)	3IJE/4G1M for Cα atoms (Å)
PSI	1−56, 434, 435	1.9	1.4
hybrid	57−108, 353−433	1.4	0.5
βI	109−352	1.3	0.7
I-EGF1	436−472	1.9	1.3
I-EGF2	473−522	2.9	1.4
I-EGF3	523−559	1.2	0.6
I-EGF4	560−600	1.5	0.8
ankle	601−605	0.4	0.2
β-tail	606−690	1.3	0.7
linker	691, 692	1.5	2.1
β-propeller	1−438	0.8	0.3
thigh	439−594	1.3	0.6
calf-1	595−737	1.8	0.9
calf-2	738−954	1.5	1.1
linker	955−959	2.0	1.6
overall		1.4	0.8

[a]The rmsd was calculated using the rms_cur command of PyMol.

Lack of a Difference between the SDLs of $\alpha_V\beta_3$ and $\alpha_{IIb}\beta_3$. The specificity-determining loop (SDL) extends from the βI domain at its interface with the β-propeller domain. It is located just outside the binding footprint for small peptide ligands and, on the basis of exchange between different integrin β-subunits, contributes to the binding of macromolecular ligands.[36] All previous $\alpha_V\beta_3$ structures (Figure 4A) differ from all $\alpha_{IIb}\beta_3$ structures (Figure 4D) over β_3 SDL residues 168−176 in structure-to-sequence register, and by the absence and presence, respectively, of two *cis*-peptides in the SDL at Ser-162/Pro-163 and Ser-168/Pro-169 (Figure 4A,D). We wondered if these differences were induced by differences between the α_{IIb} and α_V β-propeller domains with which the SDL associates. However, inspection of the electron density for the previous $\alpha_V\beta_3$-1TM structure[14] reveals clear signatures for both *cis*-Pro and a sequence-to-structure shift (Figure 4E). For example, negative density on the carbonyl group of Pro-169 when it is trans (Figure 4E) is eliminated when it is cis (Figure 4F), and positive density between the side chains of Pro-169 and Pro-170 (Figure 4E) is satisfied by the side chain of Pro-169 when it is cis (Figure 4F). Furthermore, positive densities near Glu-174, Asn-175, and Pro-176 and negative density at Leu-173 (Figure 4E) are corrected when the sequence-to-structure register is shifted and the backbone is flipped at Pro-176/Cys-177 (Figure 4F). Rebuilding to follow the electron density

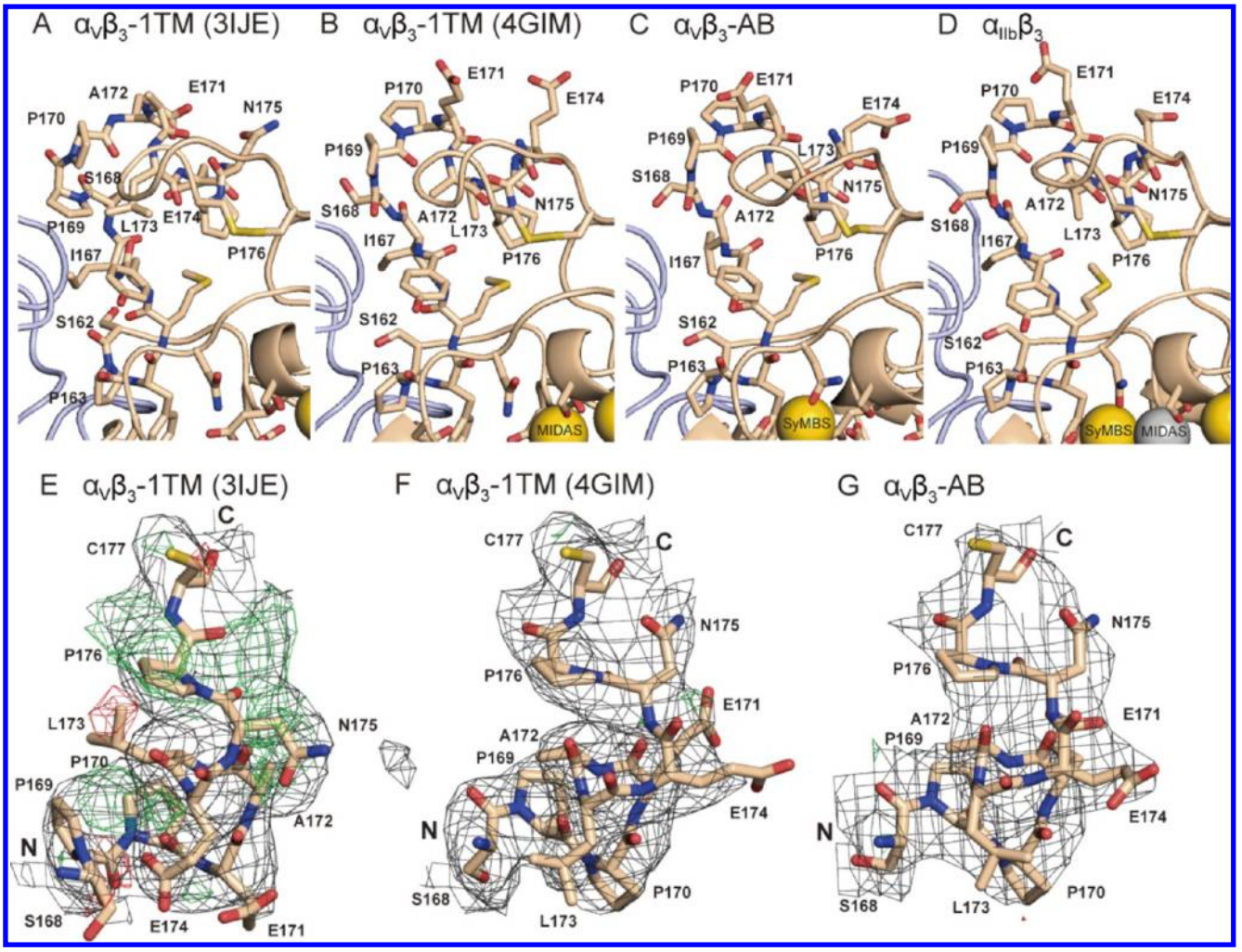

Figure 4. Conformation of the specificity-determining loop in the βI domain. The SDL and surrounding area (A–D) or a portion of the SDL (E–G) is shown for the 3IJE (A and E) and 4G1M (B and F) $\alpha_V\beta_3$-1TM structures, $\alpha_V\beta_3$-AB (C and G), and $\alpha_{IIb}\beta_3$ (D). β- and α-subunits are colored wheat and light blue, respectively. Mesh in panels E–G shows $2F_o-F_c$ electron density at 1σ (gray) or F_o-F_c difference density at 3σ (green) and -3σ (red).

resulted in SDL backbones in $\alpha_V\beta_3$-1TM (Figure 4B) and $\alpha_V\beta_3$-AB (Figure 4C) similar to that in $\alpha_{IIb}\beta_3$ (Figure 4D).

A Metal Ion at the SyMBS or MIDAS in Unliganded $\alpha_V\beta_3$. The $\alpha_V\beta_3$-AB structure has no metal at the MIDAS or ADMIDAS but has density for Ca^{2+} at the SyMBS (Figure 5A,D). The $\alpha_V\beta_3$-1TM structure has only weak density at the SyMBS, modeled as a water in 4G1M (Figure 5B). Positive density at the MIDAS in the 3IJE data set (Figure 5E) has been satisfied via placement of a Ca^{2+} ion at the MIDAS in 4G1M (Figure 5F). Thus, $\alpha_V\beta_3$-1TM has metal ions at both the MIDAS and ADMIDAS (Figure 5B). The Ca^{2+} at the MIDAS has higher *B* factors than the surrounding coordinating residues and therefore may have partial occupancy; furthermore, a water or Mg^{2+} ion (which is lacking in buffers but could have been bound to $\alpha_V\beta_3$) could also be built at the MIDAS. The most reasonable interpretation is Ca^{2+} or Mg^{2+}, both because a metal ion is normally bound here and because of the proximity of three negatively charged residues. The position of the metal ion differs from that in $\alpha_{IIb}\beta_3$, which appears to be related to the lack of metal ion binding to SyMBS in $\alpha_V\beta_3$-1TM and the consequent shift in position of the dual SyMBS- and MIDAS-coordinating residue Glu-220 (Figure 5B,C). Remarkably, the occupancy of the three βI metal ion-binding sites is completely reversed between $\alpha_V\beta_3$-AB and $\alpha_V\beta_3$-1TM (Figure 5A,B).

Overall Flexibility in the Ectodomain. Crystallographic *B* factors reflect atomic displacements in the crystal lattice and are hence related to protein flexibility. In the $\alpha_V\beta_3$-1TM backbone, *B* factors are much higher than the overall average in the I-EGF1 domain and in the N-terminal portion of the I-EGF2 domain, which connects to the I-EGF1 domain and is near the thigh domain (Figure 6A). In the $\alpha_V\beta_3$-AB backbone, *B* factors in the β_3 subunit are high in a long PSI domain loop, in the last disulfide-bonded loop of the I-EGF1 domain, and in the first loop of the I-EGF2 domain, which has a gap in continuous density (Figure 6C). In $\alpha_{IIb}\beta_3$, the first loop in the I-EGF2 domain also has high *B* factors and is partially missing in density (Figure 6E). The highest *B* factors in $\alpha_{IIb}\beta_3$ occur in the β-tail domain, which is poorly ordered (Figure 6F).

The overall position of the genu moves markedly between the two $\alpha_V\beta_3$ structures (Figure 2A,B), and the α-genu in $\alpha_V\beta_3$-AB also has high *B* factors (Figure 6C). Genu movement is tied to changes in the position of both the thigh and calf-1 domains between the two structures. The genu-proximal end of the calf-1 domain is 3.5 Å closer to the I-EGF2 domain in $\alpha_V\beta_3$-AB than in $\alpha_V\beta_3$-1TM. Furthermore, the thigh domain rotates along its long axis. Rotation is not about the center of the domain but is centered on β-strand F, which faces inward toward the lower α- and β-legs. Far from the center of rotation, the long C–D loop

dx.doi.org/10.1021/bi300734n | *Biochemistry* 2012, 51, 8814–8828

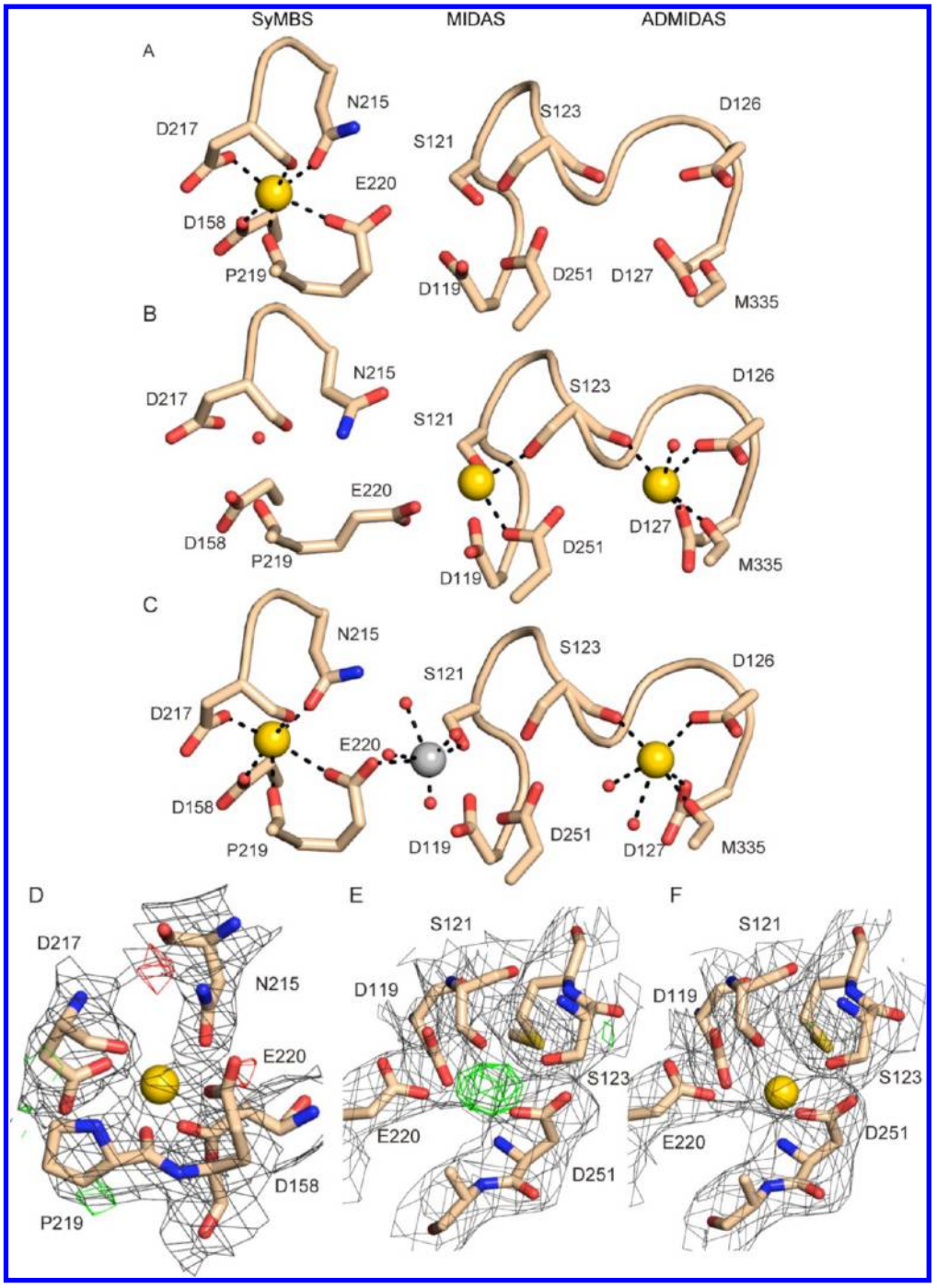

Figure 5. Metal ion-binding sites in the βI domain. (A–C) Differences in the binding of metal to the βI domain among $\alpha_V\beta_3$-AB (A), $\alpha_V\beta_3$-1TM (B), and $\alpha_{IIb}\beta_3$ (C). (D–F) Density at the metal-binding sites. (D) The SyMBS in $\alpha_V\beta_3$-AB. (E and F) The MIDAS in 3IJE (E) and 4G1M (F) $\alpha_V\beta_3$-1TM structures. Black mesh shows $2F_o-F_c$ density at 1σ, and green mesh and red mesh show F_o-F_c difference density at 3σ and -3σ, respectively. Ca^{2+} and Mg^{2+} ions are shown as gold and silver spheres, respectively. Oxygens are colored red, and waters are shown as small red spheres. Dashed lines in panels A–C show metal coordination.

in the thigh domain moves 6 Å closer to the I-EGF2 domain in $\alpha_V\beta_3$-1TM than in $\alpha_V\beta_3$-AB.

The other large movement between $\alpha_V\beta_3$-1TM and $\alpha_V\beta_3$-AB occurs in the PSI and I-EGF1 domains and in the PSI- and I-EGF1-proximal ends of the hybrid domain. While there is little change in the position of the βI-proximal end of the hybrid domain, the PSI-proximal end of the hybrid domain moves 2–2.5 Å. This libration of the hybrid domain is coupled to displacement of 2–3 Å of the PSI and I-EGF1 domains, in a direction that places the PSI and I-EGF1 domains farther from α_V in $\alpha_V\beta_3$-1TM than in $\alpha_V\beta_3$-AB.

Flexibility in I-EGF1 and I-EGF2 Domains. Flexibility occurs within I-EGF1 and I-EGF2 domains, as well as at their junctions with other domains. Cα traces shown in rainbow colors by *B* factor exhibit marked flexibility within the loops at the C-terminal end of the I-EGF1 domain and at the N-terminal end of the I-EGF2 domain, near the junctions between these domains (Figure 7). Just before the final Cys-521 of the I-EGF2

dx.doi.org/10.1021/bi300734n | *Biochemistry* 2012, 51, 8814–8828

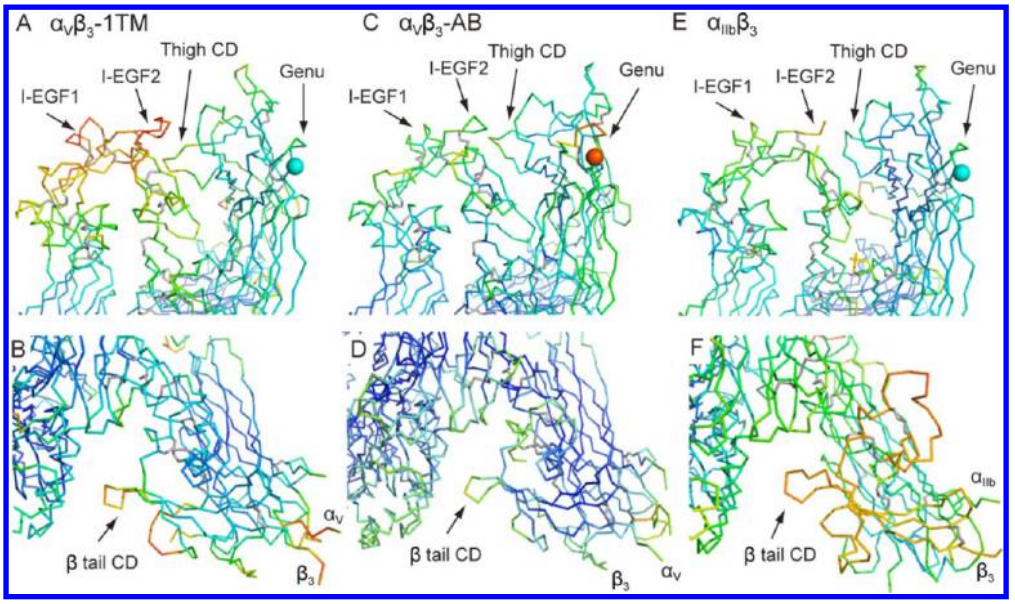

Figure 6. Flexibility among $\alpha_V\beta_3$ crystal forms and $\alpha_{IIb}\beta_3$ assessed by *B* factor distributions. The orientations are similar to those in Figure 2A−C, except in the bottom panels the integrins are rotated about the axis vertical in the page. Integrins were superimposed as in Figure 2 and separated horizontally on the page. Cα traces show *B* factors in rainbow colors, set using the lowest and highest Cα *B* factors in each integrin as the blue and red ends of the rainbow, respectively. The *B* factors shown include contributions from TLS. The genu Ca^{2+} ions are shown as spheres and also colored by *B* factor. Disulfide bonds are colored silver. The names of the α_V, α_{IIb}, and β_3 subunits are shown next to their C-termini.

domain (C8 in Figure 7E−G), Tyr-520 (Y in Figure 7E−G) participates in hydrophobic interactions with core elements of the domain and is shielded on one side by Lys-519 (K in Figure 7E−G). Tyr-520 is highly conserved as an aromatic or hydrophobic residue in the I-EGF2 domain of other integrin β-subunits. In contrast, the I-EGF1 domain lacks elements that stabilize the conformation of its C7−C8 loop and has Ser-469 and Gln-470 (S and Q in Figure 7A−D, respectively) at the sequence positions equivalent to Lys-519 and Tyr-520, respectively (Figure 7E−G).

The flexibility of the C7−C8 loop in the I-EGF1 domain is emphasized in $\alpha_{IIb}\beta_3$ headpiece structures in which the β_3 subunit terminates in the I-EGF1 domain. This loop is disordered in most such structures.[4,34] However, in recent closed headpiece structures with two headpieces per asymmetric unit,[21,35] the electron density is good enough to build most of the C7−C8 loop in one molecule and all of the C7−C8 loop in the other molecule (Figure 7D). Remarkably, this loop adopts a markedly different orientation. Although there is room in the crystal lattice for the C7−C8 loop to adopt the same conformation as seen in the complete ectodomain, as shown by superposition (Figure 7H), the C7−C8 loop instead moves to another position in the lattice, where the backbones of Pro-464 and Gly-465 participate in a network of water-mediated hydrogen bonds to the β-propeller domain of a neighboring molecule in the crystal lattice of the 2.2 Å structure.

Lack of a Stable Interface between the I-EGF2 and Thigh Domains. Substantial negative and positive $F_o - F_c$ difference density is present in the interface between the β_3 I-EGF2 and α_V thigh domains in the 3IJE $\alpha_V\beta_3$-1TM model (Figure 3A) but not in the map calculated using improved coordinates (Figure 3B). This is a region of high *B* factors, particularly in the I-EGF2 domain, but also in the extended CD loop of the α_V thigh (Figure 6A,C). Near this interface in the I-EGF1 domain, between the two $\alpha_V\beta_3$-1TM models the Cα atom positions shift 2.3 Å for Leu-467 and 1.2−1.5 Å for Gly-463, Pro-464, and Gly-465. In the C1−C2 loop of the I-EGF2 domain, at the interface with the thigh domain, the Cα atoms of Glu-475, Glu-476, Asp-477 (Figure 8A,B), Tyr-478, and Arg-479 shift 1.8, 1.8, 1.5, 1.6, and 3.5 Å, respectively, between the two models. Although these residues are more accurately located in our model, as shown by the presence of backbone density in SA composite omit maps calculated with 4G1M but not 3IJE structures (Materials and Methods), the differences in position emphasize that these are among the regions with the poorest electron density, and the most difficult to build.

The C1−C2 loop is markedly longer in the I-EGF2 domain than in other integrin I-EGF domains.[18] Several residues in this loop were too disordered to build in $\alpha_V\beta_3$-AB or $\alpha_{IIb}\beta_3$ (Figure 7E,G). Missing density here and elsewhere in the molecular model is clearly not due to proteolytic cleavage, as demonstrated by migration of the α_V and β_3 subunits at the expected molecular masses via sodium dodecyl sulfate−polyacrylamide gel electrophoresis (SDS−PAGE) (Figure S1 of the Supporting Information).

Across from the I-EGF2 domain, the electron density on the thigh side of the interface is better; nonetheless, substantial rebuilding was required to fit the density. Thus, in the interface, the Cα atoms of thigh residues Gln-504, Lys-505, Gly-506, and Glu-547 shift 1.4, 2.1, 1.4, and 3.1 Å, respectively, between the two models (see E547 in Figure 8A,B). There are no hydrogen bonds or significant hydrophobic interactions between the I-EGF2 and thigh domains in our model of $\alpha_V\beta_3$-1TM (Figure 8B), consistent with the substantial shift in orientation at the I-EGF2 domain−thigh domain interface between $\alpha_V\beta_3$-1TM and $\alpha_V\beta_3$-AB (Figure 8B,C).

Lack of a Stable Interface between the β-Tail and βI Domains. The interface between the β-tail CD (deadbolt) loop and the βI domain is extremely small in both the 4G1M $\alpha_V\beta_3$-1TM and $\alpha_V\beta_3$-AB structures, at 40 and 50 $Å^2$, respectively. Furthermore, there are no significant van der Waals interactions or hydrogen bonds between these domains. Moreover, the β-tail CD loop has high *B* factors, particularly in $\alpha_V\beta_3$-1TM (Figure 6B).

dx.doi.org/10.1021/bi300734n | *Biochemistry* 2012, 51, 8814−8828

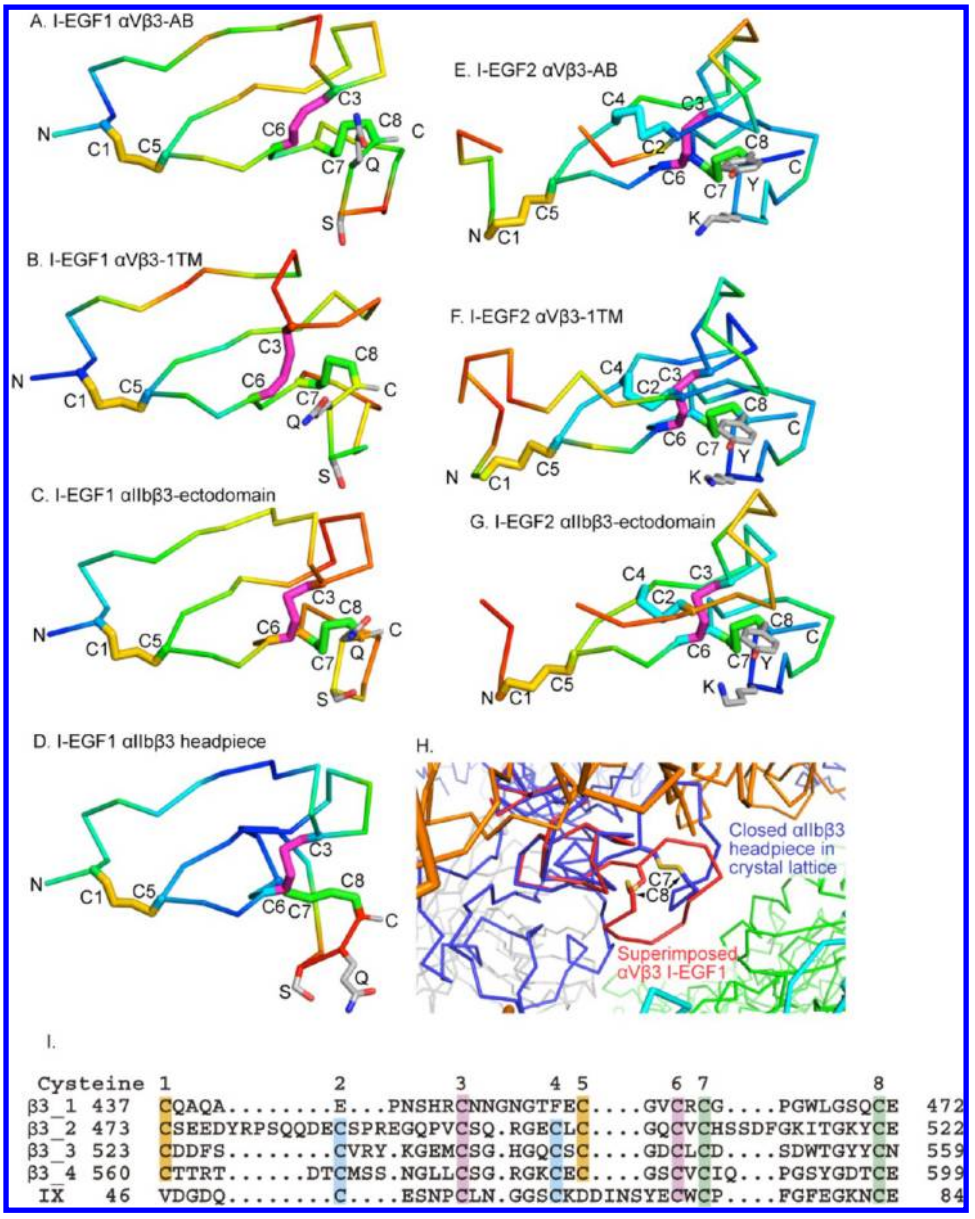

Figure 7. I-EGF domains at the β_3-knee. (A−G) I-EGF1 and I-EGF2 domains from structures determined here, the $\alpha_{IIb}\beta_3$ ectodomain,[18] or the closed $\alpha_{IIb}\beta_3$ headpiece (PDB entry 3T3P)[35] were superimposed and are shown in identical orientations aligned vertically and horizontally on the page. Cα ribbons are rainbow-colored from lowest (blue) to highest (red) Cα *B* factor in each domain. Disulfide bonds are color-coded and cysteines numbered according to the same scheme as shown in panel I. Selected side chains (S469 and Q470 in the I-EGF1 domain and the equivalent K519 and Y520 in the I-EGF2 domain) are shown. The C-terminus of the I-EGF1 domain is indicated by showing the Cα−C bond of C8 in silver. (H) The markedly different orientation of the I-EGF1 domain C7−C8 loop in a closed headpiece crystal structure (blue) is shown by superimposing the I-EGF1 domain of $\alpha_V\beta_3$-AB (red). Surrounding molecules in the closed headpiece crystal lattice are shown in different colors. (I) Sequence alignment of the β_3-integrin I-EGF domains and an EGF domain from coagulation factor IX.

Interaction of an α_V Glycopeptide Moiety with β_3. Near the furin cleavage site in the calf-2 domain of $\alpha_V\beta_3$-AB, we found a polypeptide-like electron density protruding from the calf-2 domain toward β_3, into a cavity between the I-EGF4 and β-tail domains. A second large, branched density corresponding to an N-linked carbohydrate extends from the first density. This allowed us to identify the polypeptide density as α_V residues 841−848 and to build two *N*-acetylglucosamine and four mannose residues N-linked to Asn-844 of the consensus N-glycosylation sequence (Figure 9A). Around the furin cleavage site at R860, residues 839, 840, and 849−866 are disordered.

The α_V glycopeptide moiety of residues 841−848 is inserted into a cavity between the β_3 headpiece and lower leg and forms contacts with the βI, hybrid, I-EGF4, β-ankle, and β-tail domains (Figure 9A). It is unlikely to be able to occupy the same position prior to furin cleavage. Therefore, we tested the effect on $\alpha_V\beta_3$ function of an α_V-R860A mutation. This mutation eliminated the cleavage by furin of the α_V subunit (Figure 9B). However, it had little effect on the binding of fibrinogen or fibronectin to $\alpha_V\beta_3$ transfectants measured by fluorescence flow cytometry (Figure 9C,D). In contrast, introduction of an N-linked glycan wedge into the βI domain−hybrid domain interface to favor the open headpiece conformation markedly increased the level of binding in both Ca^{2+} and Mn^{2+} (Figure 9C,D).

Linkage between the Extracellular and Transmembrane Portions of $\alpha_V\beta_3$. Improvement of the molecular model

dx.doi.org/10.1021/bi300734n | *Biochemistry* 2012, 51, 8814−8828

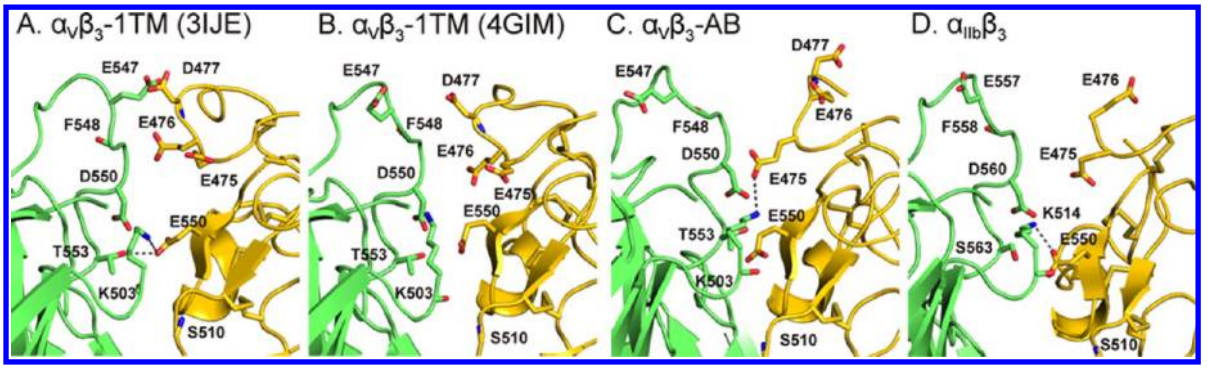

Figure 8. Lack of stable interfaces between I-EGF2 and thigh domains. Interfaces are shown in identical orientations after superposition of the ectodomains using the super command of PyMol. Thigh (green) and I-EGF2 (yellow) domains are shown with red oxygen and blue nitrogen atoms. All intersubunit hydrogen bonds found as polar contacts by PyMol are shown with dashed lines. Only 2 of the 11 hydrogen bonds shown in Figure 4D of ref 14 appear in panel A, either because highly solvated carboxyl−carboxyl and carboxyl−carbonyl interactions are considered repulsive at neutral pH or because the distances are too great; the orientations shown in Figure 4D of ref 14 differ markedly from those of the deposited 3IJE coordinates. All side chain or backbone atoms shown in Figure 4D of ref 14 are shown as sticks.

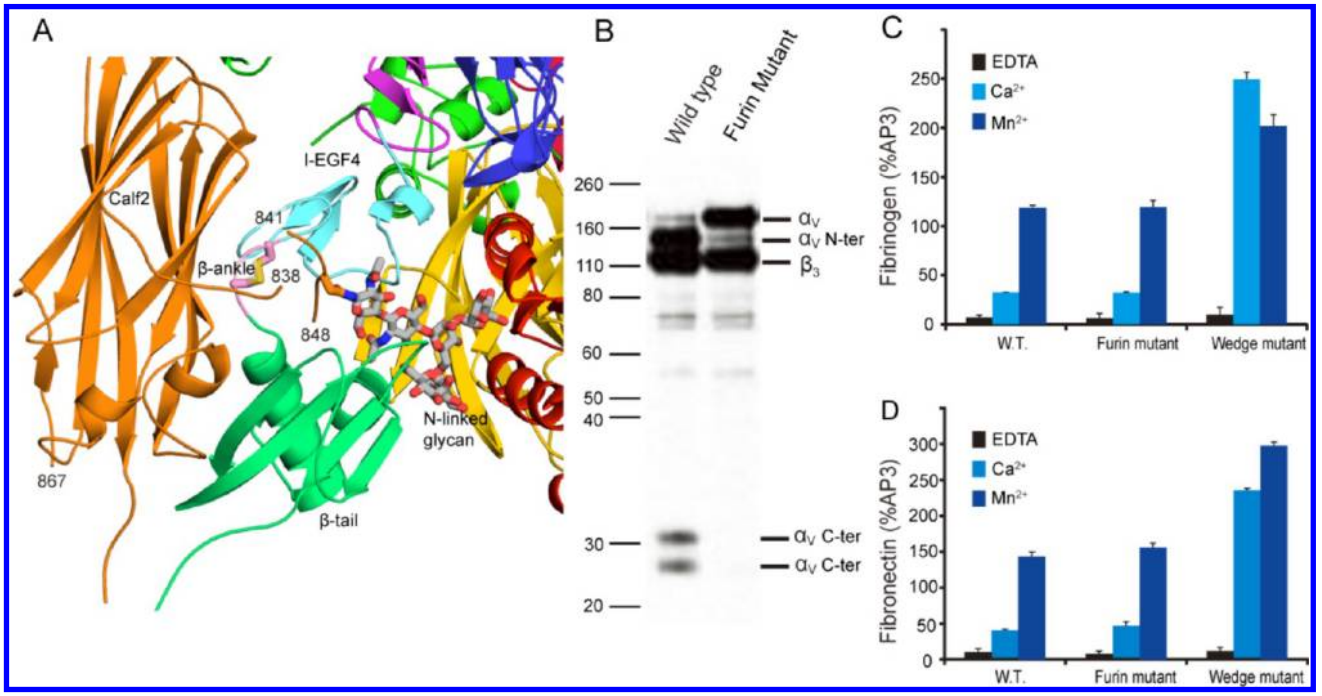

Figure 9. Interaction of an α_V glycopeptide moiety near the furin cleavage site with β_3. (A) Interaction of the glycopeptide with the β-subunit. The glycan N-linked to α_V-Asn-844 of the calf-2 domain (orange) inserts into the pocket formed by the I-EGF4 domain (light blue), the β-ankle domain (pink), the β-tail domain (green), the hybrid domain (yellow), and the βI domain (red). Carbohydrate residues are displayed with gray carbons. α_V residues 838, 841, 848, and 867 are marked, which are adjacent to positions missing in density. (B) Verification of furin cleavage site mutation by immunoprecipitation of ^{35}S-labeled $\alpha_V\beta_3$ followed by reducing SDS−7.5% PAGE and fluorography. (C and D) Binding of the ligand to cells with wild-type or mutant $\alpha_V\beta_3$ measured by fluorescence flow cytometry. Binding of fluorescently labeled fibrinogen or fibronectin to transfectants was tested in 5 mM EDTA, 5 mM Ca^{2+}, or 1 mM Mn^{2+}. The wedge mutant[8] was used as a positive control. Results are expressed as mean fluorescence intensities of the Alexa-488-conjugated ligand as a percentage of the mean fluorescence intensity of the Cy3-conjugated AP3 antibody to β_3.

of $\alpha_V\beta_3$-1TM included rebuilding of the C-terminal portion of the calf-2 domain. The backbones of L755 and G954 were rotated, and the backbone of W953 was flipped (Figure 10A,B). These changes allowed these residues to fit better into density and allowed the strong hydrogen bond between the backbones of α_V L755 and G954 to fit into continuous 1σ $2F_o-F_c$ electron density (Figure 10B). We traced generously, i.e., using 0.5σ $2F_o-F_c$ electron density, the linkers between the ectodomain and the membrane, which have high *B* factors (Figure 6B). Our $\alpha_V\beta_3$-1TM model thus extends to the A958-P959 peptide bond in α_V and the P691-D692 peptide bond in β_3 (Figure 10B). We were unable to discern any trace of the α_V and β_3 polypeptide chains beyond these positions. Thus, we were unable to build residues α_V M960−I967 or β_3 I693−V695 that were included in the 3IJE model (Figure 10A). In $\alpha_V\beta_3$-AB, we were able to build up to α_V residue P959 and β_3 residue P691 (Figure 10C).

The difficulty of tracing the $\alpha_V\beta_3$-1TM α_V linker is emphasized by the markedly different position of the A958 side chain in the two models (Figure 10A,B). The lack of experimental support for the C-terminal portion of α_V in the 3IJE model is further shown by negative 3σ F_o-F_c difference electron density on the backbone of α_V residues P957, P959, M960, P961, V962, P963, W965, and V966, as well as on the side chain of W965 (Figure 10A). Scattered 1σ $2F_o-F_c$ electron

dx.doi.org/10.1021/bi300734n | *Biochemistry* 2012, 51, 8814−8828

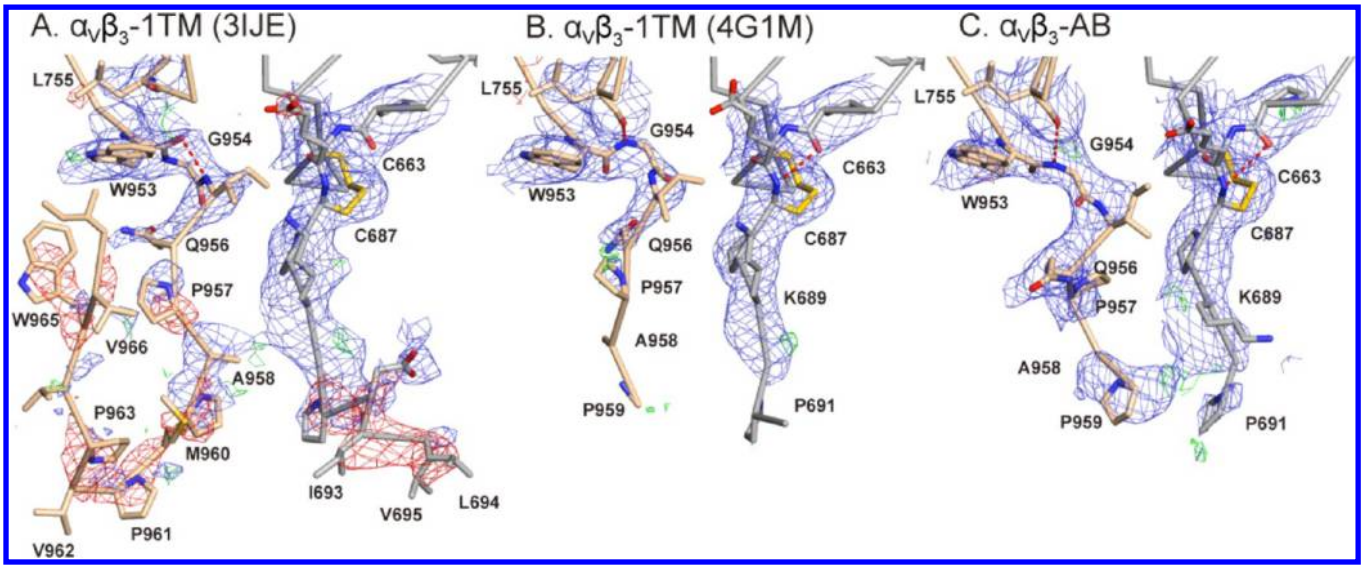

Figure 10. Structure of the linkers between the $\alpha_V\beta_3$ ectodomains and transmembrane domains: (A) 3IJE $\alpha_V\beta_3$-1TM, (B) 4G1M $\alpha_V\beta_3$-1TM, and (C) $\alpha_V\beta_3$-AB. Shown are the C-terminal α_V and β_3 extensions together with the C-terminal portions of calf-2 and β-tail domains as a Cα ribbon, together with side chains and backbones of selected regions. Hydrogen bonds near the end of the calf-2 and β-tail domains are shown as red dashed lines. Electron density is shown as mesh around α_V residues 755 and 953−967 and β_3 residues 663 and 685−695. Mesh for 1σ $2F_o-F_c$, -3σ F_o-F_c, and 3σ F_o-F_c electron density is colored blue, red, and green, respectively. CCP4 format maps were opened and displayed with the isomesh command in PyMol using carve = 2.4 and 1.9 Å for $2F_o-F_c$ and F_o-F_c maps, respectively. Mesh was calculated in panel A using 3IJE data and in panel B using 4G1M data. In panels A and B, mesh was separately calculated (carved) around the positions of atoms in both the 3IJE and 4G1M models, and the combined mesh is displayed. The view is similar to that in Figure 4A of ref 14.

density in this region of the 3IJE backbone (Figure 10A) did not appear in electron density calculated using the 4G1M model (Figure 10B), suggesting that this density was due to model bias. The absence of α_V residues 960−967 in our model eliminated negative F_o-F_c difference electron density, and positive electron density did not appear along the omitted backbone (Figure 10B).

We were also unable to build β_3 TM residues I693−V695 (Figure 10B). Continuous negative 3σ F_o-F_c electron density is present along the backbone of β_3 residues 691−695 in the 3IJE data set (Figure 10A), providing evidence against the path built for these residues. In this region of the electron density map for the 4G1M $\alpha_V\beta_3$-1TM model, no negative or positive difference electron density appears (Figure 10B).

DISCUSSION

Differences among Crystal Structures. Two crystal structures of $\alpha_V\beta_3$ have revealed unanticipated features in this well-studied integrin. The SDL is functionally important for binding macromolecular ligands.[36] Although previous structures suggested major conformational differences between this β_3 loop in $\alpha_V\beta_3$ and $\alpha_{IIb}\beta_3$, new $\alpha_V\beta_3$ structures reported here reveal no significant differences. The SDL in β_3 is thus little influenced by the associating α-subunit.

Three metal-binding sites are present at the ligand-binding site of the integrin βI domain. Density appropriate for a metal ion is present at the MIDAS in $\alpha_V\beta_3$-1TM, when phases are calculated using 3IJE or 4G1M coordinates. This contrasts with the previous assertion that no metal was present at this site in $\alpha_V\beta_3$-1TM;[14] however, our interpretation of a metal ion at the MIDAS is consistent with report of a density feature at this site in the $\alpha_V\beta_3$-ΔTM structure.[22] In $\alpha_V\beta_3$-AB, only the SyMBS is occupied, whereas in $\alpha_V\beta_3$-1TM, only the MIDAS and ADMIDAS are occupied (Figure 5). In contrast, all three metal ion-binding sites are occupied in unliganded $\alpha_{IIb}\beta_3$ crystal structures.[18,21] The SyMBS had previously been designated the LIMBS, for ligand-induced or -associated metal-binding site.[20] However, our $\alpha_V\beta_3$-AB structure clearly demonstrates that ligand binding is not required for occupancy of this site, supporting earlier observations with $\alpha_{IIb}\beta_3$ and the SyMBS designation.[18,21] Previous studies have shown that binding of Ca^{2+} to the SyMBS and Mg^{2+} to the MIDAS is synergistic;[37] this synergism can be explained both by the proximity of these two metal ion-binding sites and by the bidentate coordination of the Glu-220 side chain to both the SyMBS and ADMIDAS metal ions (Figure 5C).

The striking differences between metal ion binding to identical β_3 subunits in $\alpha_V\beta_3$ and $\alpha_{IIb}\beta_3$ may be due to crystallization conditions. The use of both Mg^{2+} and Ca^{2+} in $\alpha_{IIb}\beta_3$[18,21] and $\alpha_V\beta_3$-AB crystals and only Ca^{2+} or only Mn^{2+} in $\alpha_V\beta_3$-ΔTM and $\alpha_V\beta_3$-1TM crystals[14,20,22,33] may be one factor. The use of PEG and ammonium sulfate as precipitants in crystallization of $\alpha_V\beta_3$-1TM and $\alpha_V\beta_3$-AB, respectively, may also contribute to differences. The different pH ranges at which $\alpha_V\beta_3$ and $\alpha_{IIb}\beta_3$ crystallize may be the major factor. $\alpha_V\beta_3$-ΔTM crystallized at pH 6.0;[22] $\alpha_V\beta_3$-1TM was variously reported to crystallize at pH 5.5 in the publication or pH 4.8 in the deposited coordinates,[14] and $\alpha_V\beta_3$-AB crystallized at pH 5.8. Among $\alpha_{IIb}\beta_3$ structures in the absence of ligand, the complete ectodomain crystallized at pH 7.0[18] and the headpiece at pH 8.9.[21] Asp and Glu have pK values of 3.9 and 4.3, respectively. When these residues are close to other negatively charged residues, as they are at the SyMBS, MIDAS, and ADMIDAS, Coulomb's law dictates an increase in pK.[38] This effect could easily result in substantial protonation of metal-coordinating residues in the pH range of 4.8−6.0 used in crystallization of $\alpha_V\beta_3$ and hinder occupation of metal-binding sites. In contrast, the same residues would be more ionized at the physiologic pH of 7.4, and at pH 7.0 and 8.9 as used in $\alpha_{IIb}\beta_3$ crystallization. In contrast to the βI domain sites, the β-propeller β-hairpin Ca^{2+}-

dx.doi.org/10.1021/bi300734n | Biochemistry 2012, 51, 8814−8828

binding sites and genu are well-occupied in $\alpha_V\beta_3$ crystals. This difference can be easily explained by the close spatial relationship of the SyMBS, MIDAS, and ADMIDAS to one another.[38] Furthermore, the MIDAS and ADMIDAS have more water coordinations than any of the other integrin metal ions.

These observations suggest that the lack of simultaneous binding of metal ions to all three βI domain sites in $\alpha_V\beta_3$ is most simply explained as an artifact of crystallization conditions. An alternate explanation, that the side chain of SyMBS residue Asp-217 orients differently in $\alpha_V\beta_3$ than in $\alpha_{IIb}\beta_3$,[14] encounters the following issues: (1) either orientation fits the electron density at 2.9 Å and we have built the same orientation in $\alpha_V\beta_3$-1TM and $\alpha_V\beta_3$-AB as in $\alpha_{IIb}\beta_3$, (2) the orientation we have built is required to coordinate the SyMBS metal ion and satisfy all six octahedral coordination positions, (3) Figure 2B of ref 20 shows Asp-217 of $\alpha_V\beta_3$-ΔTM in the same orientation as we have built in $\alpha_V\beta_3$-1TM, and (4) the Asp-217 orientation built in the 3IJE model is disfavored by overlap of the electron orbitals of Oδ1 of β_3 Asp-217 and Oδ1 of α_V Asp-219, which are only 2.8 Å apart.

The concept that Ca^{2+} and Mg^{2+} bind synergistically at the SyMBS and MIDAS[18] and that, under low-pH conditions with $\alpha_V\beta_3$, metal binding and ligand binding are also synergistic is more plausible than the concept that ligand binding is regulated by or induces metal ion binding.[39] It would be difficult for the Asp of RGD to bind to the MIDAS in the absence of a metal ion and in the face of strong repulsion from negatively charged MIDAS residues. Furthermore, the SyMBS is buried, and the access of metal ions to this site would be further limited after ligand binding.

The remarkable contact of a furin cleavage site-proximal α_V glycopeptide moiety with the β_3 subunit seen here might also be dependent on crystallization conditions. $(NH_4)_2SO_4$ was the $\alpha_V\beta_3$-AB precipitant, whereas in the $\alpha_V\beta_3$-1TM crystal structure with the PEG precipitant, no density for a similar glycopeptide moiety is discernible. These differences are in agreement with the highly polar interactions of the α_V glycopeptide moiety with β_3, which are expected to be easily replaced with water or PEG. We found no effect of furin cleavage on basal or Mn^{2+}-stimulated $\alpha_V\beta_3$ ligand binding, although effects might emerge in other assays. Mutational elimination of furin cleavage sites has little effect on ligand binding in $\alpha_{IIb}\beta_3$ or $\alpha_4\beta_1$[40,41] but is required for inside-out stimulation of adhesion by $\alpha_6\beta_1$.[42]

Implications for Integrin Activation. A deadbolt model proposed that removing β-tail domain constraints from the βI domain could induce integrin activation without extension.[43] In the original proposal of this hypothesis, it was acknowledged that the β-tail domain CD or "deadbolt" loop had high temperature factors, buried a very small surface area on the βI domain, and was unlikely to contribute stabilizing energy in the conformation seen in the $\alpha_V\beta_3$-ΔTM structure; therefore, it was suggested that minor rearrangements might result in a larger interface in intact $\alpha_V\beta_3$ on the cell surface.[43] However, deletion of the β-tail domain CD loop has no activating effect whatsoever on $\alpha_V\beta_3$ and $\alpha_{IIb}\beta_3$ on cell surfaces.[44] Moreover, despite the negligible contact between the β-tail CD loop and the βI domain in $\alpha_V\beta_3$-ΔTM, there is even less in $\alpha_V\beta_3$-1TM, none in $\alpha_V\beta_3$-AB where the CD loop is disordered, and none in $\alpha_{IIb}\beta_3$.[18]

Another interface, between the α_V thigh domain and β_3 I-EGF2 domains, was recently proposed to be an energetic barrier that, when overcome, could allow $\alpha_V\beta_3$ activation in the absence of extension.[14] However, electron density is poor at this interface. We found it necessary to substantially rebuild PSI, I-EGF1, and I-EGF2 domains and loops in the thigh domain adjacent to the I-EGF2 domain in our $\alpha_V\beta_3$-1TM model. Cα atom positions in loops relevant to a proposed interface are shifted substantially between the 3IJE and 4G1M $\alpha_V\beta_3$-1TM models. Furthermore, the side chain orientations shown in Figure 4D in ref 14 are inconsistent with the associated 3IJE coordinate file and suggest that different coordinate files were used for figure preparation and coordinate deposition. Thus, Figure 4D of ref 14 but not the 3IJE coordinates (Figure 8A) show hydrogen bonds between the α_V Glu-547 side chain and the β_3 Asp-477 backbone and between the α_V Phe-548 backbone and the β_3 Glu-476 side chain. However, questionable hydrogen bonds between the side chains of α_V Asp-550 and β_3 Glu-500 and between the backbone carbonyl of α_V Glu-547 and the side chain of β_3 Glu-476 remain in the 3IJE coordinate file (Figure 8A). The 4G1M $\alpha_V\beta_3$-1TM coordinate file lacks favorable as well as unfavorable polar interactions in the same region (Figure 8B). The lack of a stable interface here and its irrelevance for regulation of the integrin affinity state are further supported by its marked reorientation in $\alpha_V\beta_3$-AB (Figure 8C), with no attendant reshaping of the βI domain ligand-binding site. These results are consistent with extensive mutagenesis evidence that the loop between cysteines 1 and 2 of the I-EGF2 domain acts as an entropic spring and that its length, but not its sequence, is important in regulating the equilibrium between bent and extended integrin conformations.[45]

In $\alpha_V\beta_3$-1TM, we were unable to trace α_V linker residues Met-960−Pro-963, α_V TM residues Val-964−Ile-967, or β_3 TM residues Ile-693−Val-695. Strong evidence against the placement of α_V residues 960−967 and β_3 residues 693−695 is shown by the presence of 3σ negative difference electron density along this backbone and on the side chain of α_V Trp-965 in 3IJE (Figure 10A), and the lack of appearance of positive difference electron density in the corresponding regions of the 4G1M $\alpha_V\beta_3$-1TM model (Figure 10B). Flexibility in the α_V and β_3 linkers is further evidenced by differences in orientation between $\alpha_V\beta_3$-1TM and $\alpha_V\beta_3$-AB beginning with α_V residue Gln-956 and β_3 residue Lys-689 (Figure 10B,C).

Flexibility of ectodomain linker residues α_V 956−963 and β_3 689−692 is to be expected from the lack of stabilizing interactions in the linker structures (Figure 10B,C). The last residue well supported by structural interactions in α_V is G954, which has a backbone hydrogen bond to L755 (Figure 10B,C). Similarly, the last such residue in β_3 is C687, which is disulfide-bonded to C663 (Figure 10B,C).

Our conclusion that the α_V and β_3 linkers are flexible is in excellent agreement with a similar lack of density for the corresponding regions in $\alpha_{IIb}\beta_3$ and $\alpha_X\beta_2$ crystal structures.[18,19] Furthermore, the use of disulfide cross-linking restraints in the linker regions of intact $\alpha_{IIb}\beta_3$ on cell surfaces showed that the α_{IIb} and β_3 linkers are flexible and, even without any motions internal to the bent conformation of $\alpha_{IIb}\beta_3$, allow marked change in the orientation of the ectodomain with respect to the membrane.[15] However, there are limits to linker flexibility; coupling of conformational change between extracellular and TM domains is disrupted by insertions of 10 or 11 extra residues.[15,46] The finding that signals can be transmitted across membranes despite the flexibility of extracellular linkers has also emerged in the epidermal growth factor receptor field, where spatial proximity between two monomers, rather than precise orientation, is important in transmembrane signaling by dimers.[47]

We also reveal differences in positions of the structured domains in the two snapshots of the ectodomain in $\alpha_V\beta_3$-1TM

and $\alpha_V\beta_3$-AB. A large number of leg domains, three in α and six in β, intervene between integrin ligand-binding domains and the ectodomain−TM domain linkers. As demonstrated by the variation in orientation between these leg domains in $\alpha_V\beta_3$-1TM and $\alpha_V\beta_3$-AB (Tables S1 and S2 of the Supporting Information), changes in TM domain orientation could be dissipated by changes in leg domain orientation. Any alternative theory of integrin activation within the bent conformation should propose a specific interdomain pathway for signal transmission, and a change in orientation between the α- and β-subunit TM domains sufficiently large in magnitude to prevent damping of transmission by ectodomain flexibility. The only specific pathway in the ectodomain described to date for transmitting conformational change to the ligand-binding site is through hybrid domain swing-out.[4] Such a large conformational change, including a 70 Å increase in the separation at the knees, is incompatible with maintenance of a compact, bent conformation.

Many mutational studies of α_V and β_3 support the importance of integrin extension, lower leg separation, and headpiece opening in integrin activation. Interfaces between the α_V and α_{IIb} calf-2 domain and β_3 I-EGF4, β-ankle, and β-tail domains are required for maintaining the low-affinity state; these interfaces prevent lower-leg separation.[48,49] Interfaces between the hybrid domain and β-tail domain[50] and between the α_V β-propeller domain and the upper β-leg domain[51] stabilize the low-affinity state by preventing integrin extension. Mutations that open disulfide-bonded loops in the I-EGF domains[52,53] or introduce bulky residues[54] or N-glycosylation sites[55] into portions of the β-leg that are buried in the bent conformation activate $\alpha_V\beta_3$ and $\alpha_{IIb}\beta_3$; these mutations destabilize the bent conformation. Mutational introduction of disulfides to prevent integrin extension,[2,56] headpiece opening,[2,56] or lower-leg separation[56] abolishes activation of $\alpha_V\beta_3$. Stabilizing the open headpiece relative to the closed headpiece with glycan wedges or computationally predicted mutations stimulated $\alpha_V\beta_3$ and $\alpha_{IIb}\beta_3$ integrin activation and LIBS epitope exposure.[8,57] Conversely, stabilizing the closed headpiece with a disulfide bond in the βI domain or computationally predicted mutations inhibited activation.[57,58]

In summary, extensive mutagenesis and structural studies of $\alpha_V\beta_3$ and $\alpha_{IIb}\beta_3$ have demonstrated the importance of multiple interfaces between the integrin headpiece and lower legs and between the integrin α- and β-legs that are present in the bent conformation and restrain integrin activation. These interfaces involve large buried surface areas and well-ordered side chains and thus contrast with the interfaces discussed above between the β-tail and βI domains and between the α- and β-knees. Integrin extension, lower-leg separation, and headpiece opening have each been shown to be required for integrin activation. The structures described here provide a sound foundation for an improved understanding of the complex molecular mechanisms that regulate integrin activation.

■ ASSOCIATED CONTENT

Supporting Information

SDS−PAGE of $\alpha_V\beta_3$ crystals (Figure S1). Differences in interdomain angles among $\alpha_V\beta_3$ and $\alpha_{IIb}\beta_3$ structures (Table S1). Disulfides as markers of differences in domain positions within superimposed $\alpha_V\beta_3$ and $\alpha_{IIb}\beta_3$ structures (Table S2). This material is available free of charge via the Internet at http://pubs.acs.org.

■ AUTHOR INFORMATION

Corresponding Author

*Address: 3 Blackfan Circle, Rm. 3100, Boston, MA 02115. Phone: (617) 713-8200. E-mail: springer@idi.harvard.edu.

Funding

Supported by National Institutes of Health Grant HL103526.

Notes

The authors declare no competing financial interest.

■ ABBREVIATIONS

MIDAS, metal ion-dependent adhesion site; ADMIDAS, adjacent to MIDAS; SyMBS, synergistic metal-binding site; TM, transmembrane; LIBS, ligand-induced binding site; EM, electron microscopy; FRET, fluorescence resonance energy transfer; SAXS, small-angle X-ray scattering; PDB, Protein Data Bank; TEV, tobacco etch virus; APS, Advanced Photon Source; MR, molecular replacement; ML, maximum likelihood; NMR, nuclear magnetic resonance; rmsd, root-mean-square deviation; SDL, specificity-determining loop.

■ REFERENCES

(1) Springer, T. A., and Dustin, M. L. (2012) Integrin inside-out signaling and the immunological synapse. *Curr. Opin. Cell Biol. 24*, 107−115.

(2) Takagi, J., Petre, B. M., Walz, T., and Springer, T. A. (2002) Global conformational rearrangements in integrin extracellular domains in outside-in and inside-out signaling. *Cell 110*, 599−611.

(3) Takagi, J., Strokovich, K., Springer, T. A., and Walz, T. (2003) Structure of integrin $\alpha_5\beta_1$ in complex with fibronectin. *EMBO J. 22*, 4607−4615.

(4) Xiao, T., Takagi, J., Wang, J.-h., Coller, B. S., and Springer, T. A. (2004) Structural basis for allostery in integrins and binding of fibrinogen-mimetic therapeutics. *Nature 432*, 59−67.

(5) Luo, B.-H., Strokovich, K., Walz, T., Springer, T. A., and Takagi, J. (2004) Allosteric β1 integrin antibodies that stabilize the low affinity state by preventing the swing-out of the hybrid domain. *J. Biol. Chem. 279*, 27466−27471.

(6) Chen, X., Xie, C., Nishida, N., Li, Z., Walz, T., and Springer, T. A. (2010) Requirement of open headpiece conformation for activation of leukocyte integrin $\alpha_X\beta_2$. *Proc. Natl. Acad. Sci. U.S.A. 107*, 14727−14732.

(7) Schurpf, T., and Springer, T. A. (2011) Regulation of integrin affinity on cell surfaces. *EMBO J. 30*, 4712−4727.

(8) Luo, B.-H., Springer, T. A., and Takagi, J. (2003) Stabilizing the open conformation of the integrin headpiece with a glycan wedge increases affinity for ligand. *Proc. Natl. Acad. Sci. U.S.A. 100*, 2403−2408.

(9) Mould, A. P., Barton, S. J., Askari, J. A., McEwan, P. A., Buckley, P. A., Craig, S. E., and Humphries, M. J. (2003) Conformational changes in the integrin βA domain provide a mechanism for signal transduction via hybrid domain movement. *J. Biol. Chem. 278*, 17028−17035.

(10) Kim, M., Carman, C. V., and Springer, T. A. (2003) Bidirectional transmembrane signaling by cytoplasmic domain separation in integrins. *Science 301*, 1720−1725.

(11) Luo, B.-H., Springer, T. A., and Takagi, J. (2004) A specific interface between integrin transmembrane helices and affinity for ligand. *PLoS Biol. 2*, 776−786.

(12) Zhu, J., Carman, C. V., Kim, M., Shimaoka, M., Springer, T. A., and Luo, B.-H. (2007) Requirement of α and β subunit transmembrane helix separation for integrin outside-in signaling. *Blood 110*, 2475−2483.

(13) Adair, B. D., Xiong, J. P., Maddock, C., Goodman, S. L., Arnaout, M. A., and Yeager, M. (2005) Three-dimensional EM structure of the ectodomain of integrin $\alpha_V\beta_3$ in a complex with fibronectin. *J. Cell Biol. 168*, 1109−1118.

(14) Xiong, J. P., Mahalingham, B., Alonso, J. L., Borrelli, L. A., Rui, X., Anand, S., Hyman, B. T., Rysiok, T., Muller-Pompalla, D., Goodman, S.

L., and Arnaout, M. A. (2009) Crystal structure of the complete integrin $\alpha_V\beta_3$ ectodomain plus an α/β transmembrane fragment. *J. Cell Biol. 186*, 589−600.
(15) Zhu, J., Luo, B. H., Barth, P., Schonbrun, J., Baker, D., and Springer, T. A. (2009) The structure of a receptor with two associating transmembrane domains on the cell surface: Integrin $\alpha_{IIb}\beta_3$. *Mol. Cell 34*, 234−249.
(16) Lau, T. L., Kim, C., Ginsberg, M. H., and Ulmer, T. S. (2009) The structure of the integrin $\alpha_{IIb}\beta_3$ transmembrane complex explains integrin transmembrane signalling. *EMBO J. 9*, 1351−1361.
(17) Yang, J., Ma, Y. Q., Page, R. C., Misra, S., Plow, E. F., and Qin, J. (2009) Structure of an integrin $\alpha_{IIb}\beta_3$ transmembrane-cytoplasmic heterocomplex provides insight into integrin activation. *Proc. Natl. Acad. Sci. U.S.A. 106*, 17729−17734.
(18) Zhu, J., Luo, B. H., Xiao, T., Zhang, C., Nishida, N., and Springer, T. A. (2008) Structure of a complete integrin ectodomain in a physiologic resting state and activation and deactivation by applied forces. *Mol. Cell 32*, 849−861.
(19) Xie, C., Zhu, J., Chen, X., Mi, L., Nishida, N., and Springer, T. A. (2010) Structure of an integrin with an α I domain, complement receptor type 4. *EMBO J. 29*, 666−679.
(20) Xiong, J. P., Stehle, T., Zhang, R., Joachimiak, A., Frech, M., Goodman, S. L., and Arnaout, M. A. (2002) Crystal structure of the extracellular segment of integrin $\alpha_V\beta_3$ in complex with an Arg-Gly-Asp ligand. *Science 296*, 151−155.
(21) Zhu, J., Zhu, J., Negri, A., Provasi, D., Filizola, M., Coller, B. S., and Springer, T. A. (2010) The closed headpiece of integrin $\alpha_{IIb}\beta_3$ and its complex with an $\alpha_{IIb}\beta_3$-specific antagonist that does not induce opening. *Blood 116*, 5050−5059.
(22) Xiong, J.-P., Stehle, T., Diefenbach, B., Zhang, R., Dunker, R., Scott, D. L., Joachimiak, A., Goodman, S. L., and Arnaout, M. A. (2001) Crystal structure of the extracellular segment of integrin $\alpha_V\beta_3$. *Science 294*, 339−345.
(23) O'Shea, E. K., Lumb, K. J., and Kim, P. S. (1993) Peptide 'Velcro*': Design of a heterodimeric coiled coil. *Curr. Biol. 3*, 658−667.
(24) Zhou, N. E., Kay, C. M., and Hodges, R. S. (1993) Disulfide bond contribution to protein stability: Positional effects of substitution in the hydrophobic core of the two-stranded α-helical coiled-coil. *Biochemistry 32*, 3178−3187.
(25) Kabsch, W. (2001) Chapter 25.2.9 XDS. In *International Tables for Crystallography* (Rossmann, M. G., and Arnold, E., Eds.) pp 730−734, Crystallography of Biological Macromolecules, Kluwer Academic Publishers, Dordrecht, The Netherlands.
(26) Adams, P. D., Afonine, P. V., Bunkoczi, G., Chen, V. B., Davis, I. W., Echols, N., Headd, J. J., Hung, L. W., Kapral, G. J., Grosse-Kunstleve, R. W., McCoy, A. J., Moriarty, N. W., Oeffner, R., Read, R. J., Richardson, D. C., Richardson, J. S., Terwilliger, T. C., and Zwart, P. H. (2010) PHENIX: A comprehensive Python-based system for macromolecular structure solution. *Acta Crystallogr. D66*, 213−221.
(27) Emsley, P., and Cowtan, K. (2004) Coot: Model-building tools for molecular graphics. *Acta Crystallogr. 60*, 2126−2132.
(28) Karplus, P. A., and Diederichs, K. (2012) Linking crystallographic model and data quality. *Science 336*, 1030−1033.
(29) Brunger, A. T., Adams, P. D., Clore, G. M., DeLano, W. L., Gros, P., Grosse-Kunstleve, R. W., Jiang, J.-S., Kuszewski, J., Nilges, M., Pannu, N. S., Read, R. J., Rice, L. M., Simonson, T., and Warren, G. L. (1998) Crystallography & NMR System: A new software suite for macromolecular structure determination. *Acta Crystallogr. D54*, 905−921.
(30) Davis, I. W., Leaver-Fay, A., Chen, V. B., Block, J. N., Kapral, G. J., Wang, X., Murray, L. W., Arendall, W. B., III, Snoeyink, J., Richardson, J. S., and Richardson, D. C. (2007) MolProbity: All-atom contacts and structure validation for proteins and nucleic acids. *Nucleic Acids Res. 35*, W375−W383.
(31) Murshudov, G. N., Vagin, A. A., and Dodson, E. J. (1997) Refinement of macromolecular structures by the maximum-likelihood method. *Acta Crystallogr. 53*, 240−255.
(32) Hodel, A., Kim, S.-H., and Brünger, A. T. (1992) Model bias in macromolecular crystal structures. *Acta Crystallogr. A48*, 851−858.
(33) Xiong, J. P., Stehle, T., Goodman, S. L., and Arnaout, M. A. (2004) A novel adaptation of the integrin PSI domain revealed from its crystal structure. *J. Biol. Chem. 279*, 40252−40254.
(34) Springer, T. A., Zhu, J., and Xiao, T. (2008) Structural basis for distinctive recognition of fibrinogen by the platelet integrin $\alpha_{IIb}\beta_3$. *J. Cell Biol. 182*, 791−800.
(35) Zhu, J., Choi, W.-S., McCoy, J. G., Negri, A., Zhu, J., Naini, S., Li, J., Shen, M., Huang, W., Bougieaaa, D., Rasmussen, M., Aster, R., Thomas, C. J., Filizola, M., Springer, T. A., and Coller, B. S. (2012) Structure-guided design of a high affinity platelet integrin $\alpha_{IIb}\beta_3$ receptor antagonist that disrupts Mg^{2+} binding to the MIDAS. *Sci. Transl. Med. 4*, 125ra132.
(36) Takagi, J., Kamata, T., Meredith, J., Puzon-McLaughlin, W., and Takada, Y. (1997) Changing ligand specificities of $\alpha_V\beta_1$ and $\alpha_V\beta_3$ integrins by swapping a short diverse sequence of the β subunit. *J. Biol. Chem. 272*, 19794−19800.
(37) Chen, J. F., Salas, A., and Springer, T. A. (2003) Bistable regulation of integrin adhesiveness by a bipolar metal ion cluster. *Nat. Struct. Biol. 10*, 995−1001.
(38) Pace, C. N., Grimsley, G. R., and Scholtz, J. M. (2009) Protein ionizable groups: pK values and their contribution to protein stability and solubility. *J. Biol. Chem. 284*, 13285−13289.
(39) Xiong, Y. M., Haas, T. A., and Zhang, L. (2002) Identification of functional segments within the β2 I-domain of integrin $\alpha_M\beta_2$. *J. Biol. Chem. 277*, 46639−46644.
(40) Kolodziej, M. A., Gaston, V., Gonder, D., Poncz, M., and Bennett, J. S. (1991) Study of the endoproteolytic cleavage of platelet glycoprotein IIb using oligonucleotide-mediated mutagenesis. *J. Biol. Chem. 266*, 23499−23504.
(41) Teixidó, J., Parker, C. M., Kassner, P. D., and Hemler, M. E. (1992) Functional and structural analysis of VLA-4 integrin a^4 subunit cleavage. *J. Biol. Chem. 267*, 1786−1791.
(42) Delwel, G. O., Hogervorst, F., and Sonnenberg, A. (1996) Cleavage of the α6A subunit is essential for activation of the α6Aβ1 integrin by phorbol 12-myristate 13-acetate. *J. Biol. Chem. 271*, 7293−7296.
(43) Xiong, J. P., Stehle, T., Goodman, S. L., and Arnaout, M. A. (2003) New insights into the structural basis of integrin activation. *Blood 102*, 1155−1159.
(44) Zhu, J., Boylan, B., Luo, B.-H., Newman, P. J., and Springer, T. A. (2007) Tests of the extension and deadbolt models of integrin activation. *J. Biol. Chem. 282*, 11914−11920.
(45) Smagghe, B., Huang, P., Ban, Y.-E., Baker, D., and Springer, T. A. (2010) Modulation of integrin activation by an entropic spring in the β-knee. *J. Biol. Chem. 285*, 32954−32966.
(46) Xiong, Y. M., Chen, J., and Zhang, L. (2003) Modulation of CD11b/CD18 adhesive activity by its extracellular, membrane-proximal regions. *J. Immunol. 171*, 1042−1050.
(47) Lu, C., Mi, L. Z., Grey, M. J., Zhu, J., Graef, E., Yokoyama, S., and Springer, T. A. (2010) Structural evidence for loose linkage between ligand binding and kinase activation in the epidermal growth factor receptor. *Mol. Cell. Biol. 30*, 5432−5443.
(48) Kamata, T., Handa, M., Sato, Y., Ikeda, Y., and Aiso, S. (2005) Membrane-proximal α/β stalk interactions differentially regulate integrin activation. *J. Biol. Chem. 280*, 24775−24783.
(49) Donald, J. E., Zhu, H., Litvinov, R. I., DeGrado, W. F., and Bennett, J. S. (2010) Identification of interacting hot spots in the β3 integrin stalk using comprehensive interface design. *J. Biol. Chem. 285*, 38658−38665.
(50) Matsumoto, A., Kamata, T., Takagi, J., Iwasaki, K., and Yura, K. (2008) Key interactions in integrin ectodomain responsible for global conformational change detected by elastic network normal-mode analysis. *Biophys. J. 95*, 2895−2908.
(51) Vomund, A. N., Stuhlsatz-Krouper, S., Dimitry, J., Song, Y., and Frazier, W. A. (2008) A naturally occurring extracellular α-β clasp contributes to stabilization of β3 integrins in a bent, resting conformation. *Biochemistry 47*, 11616−11624.
(52) Kamata, T., Ambo, H., Puzon-McLaughlin, W., Tieu, K. K., Handa, M., Ikeda, Y., and Takada, Y. (2004) Critical Cys residues for

regulation of integrin $\alpha_{IIb}\beta_3$ are clustered in the epidermal growth factor domains of the β3 subunit. *Biochem. J. 378*, 1079−1082.
(53) Nurden, A. T., Fiore, M., Nurden, P., and Pillois, X. (2011) Glanzmann thrombasthenia: A review of ITGA2B and ITGB3 defects with emphasis on variants, phenotypic variability, and mouse models. *Blood 118*, 5996−6005.
(54) Vanhoorelbeke, K., De Meyer, S. F., Pareyn, I., Melchior, C., Plancon, S., Margue, C., Pradier, O., Fondu, P., Kieffer, N., Springer, T. A., and Deckmyn, H. (2009) The novel S527F mutation in the integrin β_3 chain induces a high affinity $\alpha_{IIb}\beta_3$ receptor by hindering adoption of the bent conformation. *J. Biol. Chem. 284*, 14917−14918.
(55) Kashiwagi, H., Tomiyama, Y., Tadokoro, S., Honda, S., Shiraga, M., Mizutani, H., Handa, M., Kurata, Y., Matsuzawa, Y., and Shattil, S. J. (1999) A mutation in the extracellular cysteine-rich repeat region of the β3 subunit activates integrins $\alpha_{IIb}\beta_3$ and $\alpha_V\beta_3$. *Blood 93*, 2559−2568.
(56) Kamata, T., Handa, M., Ito, S., Sato, Y., Ohtani, T., Kawai, Y., Ikeda, Y., and Aiso, S. (2010) Structural requirements for activation in $\alpha_{IIb}\beta_3$ integrin. *J. Biol. Chem. 285*, 38428−38437.
(57) Luo, B. H., Karanicolas, J., Harmacek, L. D., Baker, D., and Springer, T. A. (2009) Rationally designed integrin β_3 mutants stabilized in the high affinity conformation. *J. Biol. Chem. 284*, 3917−3924.
(58) Luo, B.-H., Takagi, J., and Springer, T. A. (2004) Locking the β_3 integrin I-like domain into high and low affinity conformations with disulfides. *J. Biol. Chem. 279*, 10215−10221.